Experimental and numerical investigation of spray characteristics in a new FLOX® based combustor for liquid fuels for Micro Gas Turbine Range Extender (MGT-REX).

James D. Gounder[1], Anton Zizin[2], Oliver Lammel[3], Michael Rachner[4], and Manfred Aigner[5]
German Aerospace Center (DLR) Institute for Combustion Technology, Pfaffenwaldring 38-40, 70569 Stuttgart, Germany

and

Sagar R. Kulkarni [6]
Process and Energy Department, Delft University of Technology, Delft, The Netherlands

A liquid fuel combustor based on the FLOX® gas turbine burner concept has been developed for application in a Micro Gas Turbine (MGT) Range Extender (REX) for next generation cars. The characterization of this combustor was performed at the High Pressure Optical Test rig (HIPOT) at DLR Stuttgart. Spray characteristics were measured using droplet mie scattering and phase Doppler interferometry in flames of a stable burner operation point (BOP) at a pressure, preheat temperature, global lambda (λ_G), and jet velocity of 3.5 bars, 300 °C, 1.45 and 120 m/s respectively. The experimental results showed long flames with deep penetration of the spray into the combustion chamber. A comprehensive data set of the spray characteristic with well-defined boundary condition was made available for CFD simulations. The CFD simulation of the two-phase flow was performed by coupling the DLR liquid phase simulation code SPRAYSIM with the commercial CFD-code ANSYS CFX-16.1. The comparison of axial and radial velocity profiles between simulation and experiment clearly showed that the turbulence model used in the numerical simulation was unable to predict the measured turbulence appropriately. The calculated and measured spray behavior in the combustion chamber showed satisfying agreement. The observed differences were mainly due to the simple 1-step global combustion model, which predicted an early onset of the heat release. The simulation showed that even though a large portion of the evaporation happened already inside the nozzle, the remaining spray droplets penetrate deep into the combustion chamber.

Nomenclature

C_D	*[]*	*Drag coefficient*
d	*[µm]*	*Droplet diameter*
Dmn	*[µm]*	*Mean diameters (D10, D20, D30 and D32(=SMD)) of drop size distribution*

[1] Combustion Scientist, German Aerospace Center (DLR), Institute for Combustion Technology, Pfaffenwaldring 38-40, 70569 Stuttgart, Germany and Non Member.
[2] Combustion Scientist, German Aerospace Center (DLR), Institute for Combustion Technology, Pfaffenwaldring 38-40, 70569 Stuttgart, Germany and Non Member.
[3] Combustion Scientist, German Aerospace Center (DLR), Institute for Combustion Technology, Pfaffenwaldring 38-40, 70569 Stuttgart, Germany and Non Member.
[4] Combustion Scientist, German Aerospace Center (DLR), Institute for Combustion Technology, Linder Höhe, 51147 Cologne, Germany and Non Member.
[5] Institute Director, German Aerospace Center (DLR), Institute for Combustion Technology, Pfaffenwaldring 38-40, 70569 Stuttgart, Germany, and Non Member.
[6] MSc Student, Process and Energy Department, Delft University of Technology, Delft, The Netherlands, and Non Member.

Dv	$[\mu m]$	*Volume-undersize diameters (Dv0.1, Dv0.5(=MMD), Dv0.9) of drop size distribution*
k	$[J/kg]$	*Turbulent kinetic energy*
P_{th}	$[kW]$	*Thermal power*
r	$[mm]$	*Radial distance across nozzle*
St	$[]$	*Stokes Number*
τ_d	$[s]$	*Droplet relaxation time*
τ_t	$[s]$	*Turbulent time scale*
U	$[m/s]$	*Axial mean velocity*
u'	$[m/s]$	*Axial rms velocity*
u_s	$[m/s]$	*Droplet slip velocity*
V	$[m/s]$	*Radial mean velocity*
v'	$[m/s]$	*Radial rms velocity*
v_{Jet}	$[m/s]$	*Jet velocity*
x	$[mm]$	*Axial distance along combustion chamber length (x=0 is the nozzle exit plane)*
y	$[mm]$	*Radial distance across burner*
z	$[mm]$	*Azimuthal distance across burner*

Greek Letters

ε	$[W/kg]$	*Turbulent dissipation*
λ_G	$[]$	*Global Lambda (global air-to-fuel ratio / stoichiometric air-to-fuel ratio)*
ρ	$[kg/m^3]$	*Density*

Abbreviations

BOP	*Burner Operation Point*
C	*Coincidence*
CL	*Chemiluminescence*
EDM	*Eddy Dissipation Model*
FRC	*Finite Rate Chemistry*
GT	*Gas Turbine*
HIPOT	*High Pressure Optical Test rig*
LES	*Large Eddy Simulation*
MILES	*Monotone Integrated LES*
MGT	*Micro Gas Turbine*
NC	*Non Coincidence*
PDI	*Phase Doppler Interferometry*
PIV	*Particle Image Velocimetry*
RANS	*(Steady) Reynolds-Averaged Navier Stokes Simulation*
REX	*Range Extender*
SST	*Shear Stress Turbulence model*
VLES	*Very Large Eddy Simulation*

I. Introduction

The entire automobile industry is pushing towards development of new technologies for electro mobility. One of the factors that have a negative influence on the demand for electric cars is the maximum range they can achieve in one battery charge. The goal of attaining longer range (~1000 km) even with the existing hybrid cars is difficult to reach. Thus an internal project at the German Aerospace Center (DLR) is dedicated to the development of a range extender for electric cars, which would enable future cars to attain longer range. A number of range extender concepts are being studied, and one in particular that is being developed at the Institute of Combustion Technology is based on a low emission micro gas turbine (MGT) technology. The initial design requirements specified for the MGT range extender (REX) are: it operates with liquid fuel and it can deliver approximately 48 kW of electrical power while being compact in size and meeting exhaust emission regulations. For all gas turbines (GT), the design of the combustor is the critical component that influences the emissions.

Natural gas fired stationary GT use lean premixed combustion technology in order to avoid high nitrogen oxide emissions. In most of these combustors the flames are aerodynamically stabilized by swirl. Even though the swirl

stabilized burner systems have been widely used in GT, they are also susceptible to thermo-acoustic instabilities and sensitive with respect to fuel composition changes (flame position, flashback), which limit their operation. FLOX® gas turbine combustors, on the other hand, have proven to be an alternative for reliable and fuel flexible low emission combustors[1-5]. Even though the combustion process in the FLOX® GT combustor does not meet the characteristics of flameless oxidation[6, 7], nor volume or mild combustion[8, 9] due to its high power density and high adiabatic flame temperatures[2] and it also differs from the conditions in the atmospheric furnaces at low power density[2, 9, 10]. Nevertheless, the term FLOX® denotes a certain model type of the GT burner[2, 11, 12] and this concept offers fuel flexibility, low emissions, improved part load performance and simple scalability. The key feature of FLOX® GT combustors are high momentum jets, which are discharged through orifices arranged in a circle into the combustion chamber. The axial high momentum jet flow provides distinct recirculation in the combustion chamber as shown in Fig.1 of Ref. 11 or Fig. 6 of Ref. 13. This leads to an intense mixing of burnt gas with fresh fuel/air mixtures, and thus stabilization of the flame. Flashback resistance is obtained through the absence of low velocity zones, which favors this concept for multi-fuel applications. The FLOX® burner concept has been successfully adapted to MGT operating with various gaseous fuels for electrical power output ranging from 3 kW[14] to 100 kW[15, 16] with promising results.

Implementing FLOX® combustors operating with liquid fuel to MGT generates extra challenges, as almost all MGT combustors are not capable to operate with liquid fuels in a low emission regime unless with water injection. Additional restrictions imposed on combustor design and operation by the use of liquid fuels are due to physical sizing, which can have a significant effect on processes such as atomization, evaporation, and mixing of fuel and air. In the case of a MGT application, the direct scaling of the air nozzle and atomizer size depends on the thermal power requirements, which in turn determines the injection hole size. This might result in different scaling factors for the air nozzle and the atomizer. The down-scaling of the atomizer size can lead to extremely small injection holes which are susceptible to blockages due to coking.

Zizin et al[17] initiated the basic steps of the development process of a novel combustion system for liquid fuels, based on a FLOX® GT burner for MGT-REX application. The results from the work done in Ref. 17 have been used in the design of a high pressure version of a 8 nozzle liquid FLOX® burner. Further development of this combustor requires a detailed understanding of the physical and chemical processes taking place in it. High pressure combustion test facilities with optical access and advanced diagnostics coupled with numerical tools provide an excellent platform for gaining a deeper understanding of the underlying phenomena. The high pressure optical test rig (HIPOT) at the DLR is one such facility where the 8 nozzle liquid FLOX® burner is being extensively tested. The operability limits of the liquid FLOX® burner at actual operating parameters (P = 3.5 bars and T = 300 °C) of a projected MGT-REX have been mapped by Gounder et al[18]. The exhaust gas results presented in Ref. 18 showed good promise where measured NO_x and CO levels are below 5 and 10 ppm, respectively (corrected for reference 15% O_2) at a global lambda (λ_G) of 1.89. However, the length of the flames is long, which would create huge challenges with regards to the size of the combustor. It should also be noted that this is an initial design concept that provides a starting point for the further development of a burner that would be implemented into the MGT-REX.

The simplicity of the liquid FLOX® burner geometry and layout lends itself as an ideal configuration for application of laser diagnostic experiments and the validation of numerical simulations. The fuel in the liquid FLOX® burner is injected upstream of the nozzle exit plane and the spray droplets are transported via the carrier air through the mixing tube into the combustion chamber, The use of a simple pressure atomizer and the absence of swirl simplifies the boundary conditions considerably. The first results of the spray characteristics of the liquid FLOX® burner have been presented in Ref. 18 where the effects of varying jet velocity (v_{Jet}), λ_G and thermal power (P_{th}) on the flame shape and droplet field were investigated. The measured spray length showed large penetration depth of the spray into the combustion chamber from the nozzle exit plane. In the present work one of the burner operation point (BOP) from Ref. 18 is chosen, for which detailed droplet data obtained from Phase Doppler Interferometry (PDI) measurements are provided for validation of CFD simulation.

The results from the spray measurement will be used for initial conditions for the CFD simulation as well as for comparison of measurements and computation. The CFD simulation of the two-phase flow in the domain was performed by coupling the DLR liquid phase simulation code SPRAYSIM[19-23] with the commercial CFD-code ANSYS CFX-16.1. The two-way coupling of both codes happens via interface routines. The experimental and computational results complement each other and together provide a better insight into the behavior of the spray flame for further development of the liquid FLOX® burner.

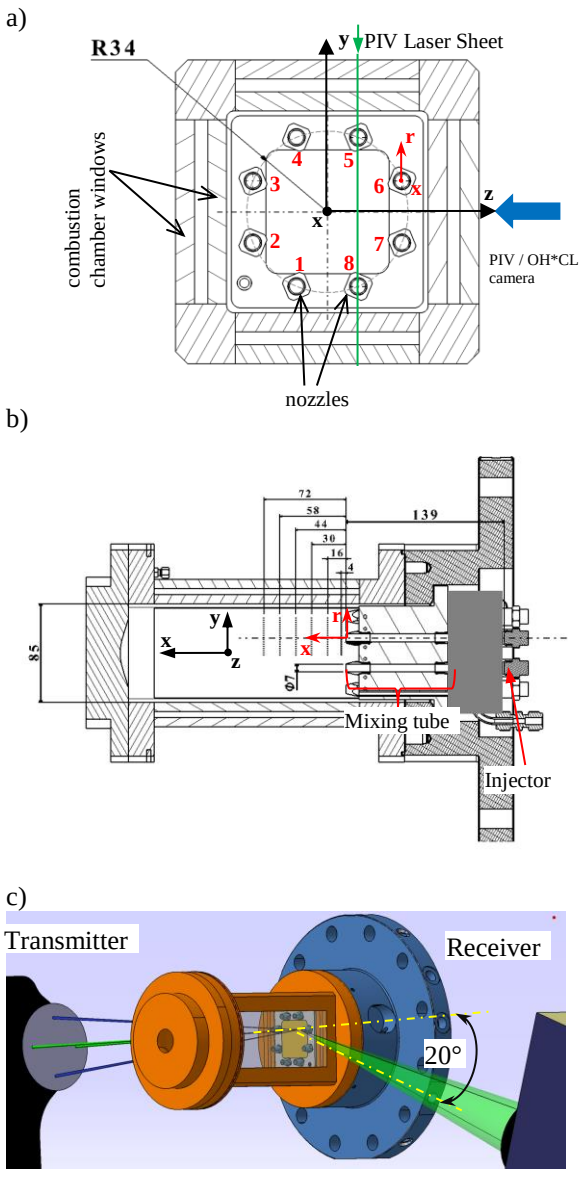

Figure 1. a) Sectioned view from the middle of the combustion chamber (yz plane) showing the arrangement of the nozzles and the PIV+Mie scattering sheet. b) Sectioned view (rx plane) of the combustion chamber across nozzles 6 & 7 showing the injector and PDI measurement locations c) Setup of the PDI transmitter and receiver for measurements over nozzle 6.

Table 1. Physical and chemical properties of the light heating oil that has been used as fuel.

Parameter	Standard	Value	Unit
Density (20°C)	DIN EN ISO 12185	833.8	Kg/m³
HHV	DIN 51900-1 mod.	45626	J/g
LHV	DIN 51900-2 mod.	42934	J/g
Kinematic Viscosity (20°C)	DIN EN ISO 3104	3.755	mm²/s
Monoaromatics	DIN EN 12916	21.8	%
Diaromatics		5.4	%
Triaromatics		0.7	%
Polyaromatics		6.1	%
Totalaromatics		27.9	%

Table 2. Initial conditions of the selected BOP for detailed analysis.

Parameter	Value
P (bars)	3.5
T_{air} (°C)	300
λ_G	1.45
v_{Jet} (m/s)	120
P_{th} (kW)	186
T_{fuel} (°C) (measured in fuel plenum)	37
Fuel mass flowrate (g/s)	4.3

II. Burner

The liquid FLOX® burner was specifically designed for testing at the HIPOT, at DLR Stuttgart. The design of this burner was based on earlier work carried out by Zizin et al[17, 18]. The main application of the burner was for operation at a thermal power (P_{th}) of 155 kW and a corresponding pressure of 3.5 bars, in order to meet the electric power output requirement of 48 kW_{el} from the MGT-REX. This 48 kW_{el} requirement was the basis for a simulated performance curve of a projected appropriate MGT.

Figure 1 a) shows the sectioned view of the burner in yz plane taken in the middle of the combustion chamber. The burner face cross section is 81 × 81 mm. The liquid FLOX® burner consists of 8 nozzles equally spaced on a circle of radius 34 mm as shown in Fig. 1 a). The burner was designed also for fuel staging and part load operations and for these purposes, injectors in nozzles 1-5 have one common fuel plenum and nozzles 6-8 have their own fuel supply. The fuel flow to the plenums can be regulated by two separate flow controllers, which is useful for

investigating fuel staging effects, or by one common fuel controller. Figure 2 b) shows a sectioned view of the combustion chamber and the burner in the xr plane across nozzle 6. The diameter of a single nozzle is 7 mm. Each nozzle is equipped with a pressure atomizer from Steinen, model 0.25-45° GPH MST MICRO-FLO, mounted 139 mm upstream of the nozzle exit plane as shown in Fig. 1 b). The atomized fuel from each injector is transported by stream of carrier air through a contraction into the mixing/pre-vaporizing tube for the respective nozzle before entering the combustion chamber. Due to a pending patent application the section between the injector and the mixing tube cannot be presented in this paper, however it will be made available once the patent application is finalized. The inlet section of the mixing tube contains carefully positioned holes, which pick up very small amounts of main air and create a thin air film along the wall of the nozzles.

The burner housing is bolted to the supply module of the HIPOT rig. The burner surface plate is cooled by impingement for high thermal loads using a small percentage of the main combustion air which is directed to the back face of the burner front plate, and re-introduced into the optical combustion chamber along the windows hence keeping the global lambda (λ_G) constant. The combustion chamber has a square cross section of 85 × 85 mm. The length of the combustion chamber is 200 mm. The windows at the sides are double quartz glass with cooling air flowing in between the two glasses. The metal parts of the combustion chamber frame are water-cooled. The exit of the combustion chamber has a diameter of 33 mm.

III. Initial Conditions

The difference in the properties of light heating oil and diesel is small[18], hence light heating oil has been used as fuel for the liquid FLOX® burner tests. A sample of the light heating oil, which was readily available at DLR, was analyzed by the company ASG Analytik-Service GmbH. The physical and chemical properties of the oil are provided in Table 1. The operability limit of the burner at 3.5 bars has been mapped out by Gounder et al[18], for global lambda (λ_G) ranging from 1.25 – 2.00 and bulk jet velocity (v_{Jet}) from 80 – 140 m/s. The resulting thermal load (P_{th}) for the given λ_G and v_{Jet} combination is in the range of 90 to 236 kW. One BOP has been selected from the operability map[18] of the liquid FLOX® burner for detailed experimental and numerical analysis. The initial conditions of the selected BOP are presented in Table 2, and it will be referred to as the test case from here onwards in the text. It should also be noted here that only one flow controller was used for the fuel supply to both fuel plenums.

IV. Optical and Laser Diagnostics

Chemiluminescence (CL) imaging of the OH* radical was used for monitoring the flame shape and length. Mie scattering of spray particles provided information on spray length and spray penetration depth into the combustion chamber. Imaging the Mie scattering signal using a double pulse laser in combination with a double frame camera system allowed for PIV measurement of the spray. The droplet size and velocity was measured using Phase Doppler Interferometry (PDI) technique. These optical and laser diagnostic techniques have been described in detail in Ref. 18 and hence only a brief description is given in the following sub sections.

A. OH* Chemiluminescence

The OH* CL signal was collected using a combination of LaVision intensifier and camera installed on one side of the test rig. The viewing angle of the OH* CL camera setup is as shown in Fig. 1 a). The signal collection optics consisted of an achromatic Halle UV lens with a focal length of 100 mm and a f/# of 2. A bandpass filter, which transmits light in the range from 290 nm to 335 nm, was mounted in front of the objective in order to filter the OH* signal. The image intensifier exposure time was set to 75 µs. For every measurement case 500 images were recorded at a recording rate of 9 Hz. Since CL is a line of sight measurement technique, 3D-effects have to be taken into account for the interpretation of the results.

B. Mie Scattering and Spray PIV

A flash lamp pumped frequency-doubled Nd:YAG laser (New Wave Solo PIV 120) was used for illuminating the spray particles. The laser was operated in double pulse mode. The laser beam was expanded into a light sheet using two cylindrical lenses ($f_1 = -22$ mm and $f_2 = 100$ mm) and a spherical lens (f = 1000 mm) before entering the combustion chamber from the top, passing through the central plane of nozzles 5 and 8 as illustrated in Fig. 1 b). The laser sheet width covered the full length of the high pressure window which is not shown here.

The camera setup for Mie scattering was similar to the OH* CL setup, except the intensifier was removed and the UV lens was replaced with a 50 mm focal length camera lens with f/# set to 16. The scattered laser light at 532

nm from the spray particles was collected with the CCD camera positioned normal to the laser sheet as shown in Fig. 1 a). The camera was operated in double frame mode. The spray length was deduced from the 1st frame of the Mie scattering image. Imaging in double frame mode with two laser pulses (Δt between pulses of 7 µs) allowed for PIV measurements to be performed using spray particles. In order to reduce background noise in the PIV images a narrow bandpass filter centered at 532 nm was fitted in front of the camera lens.

The velocity vectors were calculated using commercial PIV software, LaVision Davis 8.15. An adaptive multi pass cross correlation algorithm was used with interrogation windows ranging from 64 pixels to 32 pixels. The final PIV window size was 32 × 32 pixels with a window overlap of 50%. The field of view imaged with the PIV system was 120 × 85 mm² (H × W) which resulted in a spatial resolution and vector spacing of 1.4 mm and 0.7 mm respectively.

C. Phase Doppler Interferometry (PDI)

A Phase Doppler Interferometry (PDI) system from Artium Technologies Inc. (Model PDI-300 MD) was used for measuring droplet size and velocity. The PDI system was setup for two component (axial & radial) velocity measurements. Figure 1 c) shows the arrangement of the transmitter and receiver with respect to the combustion chamber. The main transmitter unit has two inbuilt diode pumped solid state lasers producing laser light at 532 nm (green) and 491 nm (blue) which are split into two beams of the respective wavelengths. Bragg cells fitted in the transmitter unit modulate a frequency shift to one of the beams from each pair by 40 MHz to allow measurement of velocity in the negative direction. The green beams are used for axial velocity and droplet size measurements, while the blue beams are used for radial velocity. The laser light transmission optics for the probe volume had a focal length and beam separation of 500 mm and 59 mm, respectively. The beam waist at the measurement location was approximately 241 µm and 223 µm in diameter for the two respective laser wavelengths.

The PDI signal was collected by the receiver at a 20° forward scattering configuration as shown in Fig. 1 c). The width of the windows in the pressure module of the test rig restricted the receiving angle to a maximum of 20°. A 500 mm focal length lens and a slit width of 500 µm were used for signal collection. The parameter settings of the receiver optics assembly were maintained constant for all measurements along the flame axis in order to minimize any bias in the droplet size distribution relative to results obtained at upstream locations. These settings were determined by the saturation constraints near the jet exit plane (x = 4 mm). The particular hardware and software settings allow for droplet size measurement in the range of 1 to 167 µm. Two components of the velocity, axial (U) and radial (V), of droplets and droplet diameter were measured in radial traverses over nozzle 6 at selected axial locations as shown in Fig. 1 b).

V. Numerical Approach

The numerical simulation of the two-phase flow was performed by coupling the DLR liquid phase simulation code SPRAYSIM with the commercial CFD-code ANSYS CFX-16.1. The gas field simulation was calculated using the finite volume code of CFX employing the two-equation shear stress transport (SST) model of Menter[24], whereas the Lagrangian particle tracking of the droplets was performed by SPRAYSIM. The two-way coupling of both codes with the exchange of the gas field and the spray feedback source terms was done via interface routines using the user Fortran feature of CFX.

The Fortran95-code SPRAYSIM is the development platform of the DLR Institute of Combustion Technology for unsteady or steady Lagrangian particle simulation[19-23]. It is designed basically as a standalone code running both under LINUX and WINDOWS, that can be coupled via files or online coupling via function-calls to CFD gas field codes. The code is MPI-parallelized in the number of computational particles ('parcels'). The particle tracking happens on domains with unstructured grids employing a predictor-corrector solver for the ordinary differential equations. Models for turbulent particle dispersion, atomization and multicomponent evaporation are contained within. SPRAYSIM employs registration planes, where computational parcels that pass these planes are registered during the tracing. The individual parcel data are accumulated and finally processed to obtain distributions and profiles of characteristic spray diameters, size distributions, liquid fluxes, spray velocities, temperatures, etc. This is required for a quantitative evaluation of the spray and for comparison with spray measurements.

For the present application, the spectral particle dispersion model of Blümcke[25] as well as the Abramzon and Sirignano[26] evaporation model along with a rapid mixing approach for the liquid interior was used. The light heating oil was approximated as a single component fuel $C_{14.32}H_{25.75}$ .The combustion model used is a combination of the eddy dissipation model (EDM) to account for the influence of small scale turbulent mixing on combustion, and a global 1-step finite rate chemistry (FRC) model based on Arrhenius rates. The local reaction rates [mole fuel /m^3/s] are computed by:

$$R = \min(R_{EDM}, R_{FRC}) \quad (1)$$

With

$$R_{EDM} = A_{EDM} \cdot \frac{\epsilon}{k} \cdot min\left(\left[C_xH_y\right], \frac{[O_2]}{x+\frac{y}{4}}\right) \quad (A_{EDM} = 2.0) \quad (2)$$

$$R_{FRC} = A_{FRC} * \left[C_xH_y\right]^{0.25} \quad [O_2]^{1.5} * exp(\frac{E_a}{RT})) \quad (3)$$

(A_{FRC} = 1.36e+15 , Ea=1.256e+5), where units in Arrhenius rate are J, mole, m, K.

$$C_xH_y + \left(x+\frac{y}{4}\right)O_2 \rightarrow x\,CO_2 + \frac{y}{2}H_2O \quad (x = 14.32\,,\ y = 25.75) \quad (R1)$$

This simple approach was chosen, as CFX-16.1 has only a beta feature of a solver for detailed FRC and no interface to import mechanisms in CHEMKIN format. Therefore, a 3-step global EDM/FRC model was used initially, but it yielded unrealistically large amounts of the intermediate species CO, H_2 and too low final temperatures. So the 1-step global EDM/FRC model was used. The calculation domain for the numerical RANS simulation comprised of one of the eight nozzles (nozzle #6), i.e. 1/8 of the plenum, a full premix chamber and mixing tube and 1/8 of the combustion chamber. Symmetry boundary conditions were applied at the sectorial planes of the plenum and the combustion chamber.

VI. Experimental Results

A. Flame Shape and Spray Field

The mean OH* CL, the rms image of the Mie scattering images and ensemble average of the spray velocity field measured in the flames of the test case are shown in Fig. 2. The average image of OH* CL was calculated from 500 single shot images corrected for background noise and non-uniform intensity distribution of the CCD chip. The image plane is perpendicular to the burner front plate. The heat release zones marked by OH* are a good marker of the flame shape, flame lift off height and length[27, 28]. Individual jet flames are clearly visible in the OH* CL images. The flame stabilizes close to the nozzle exit plane and the length of the flames cover almost two thirds of the combustion chamber length. The reaction zones are concentrated to the jets of individual nozzles and the peak heat release occurs between 60 mm < x < 100 mm.

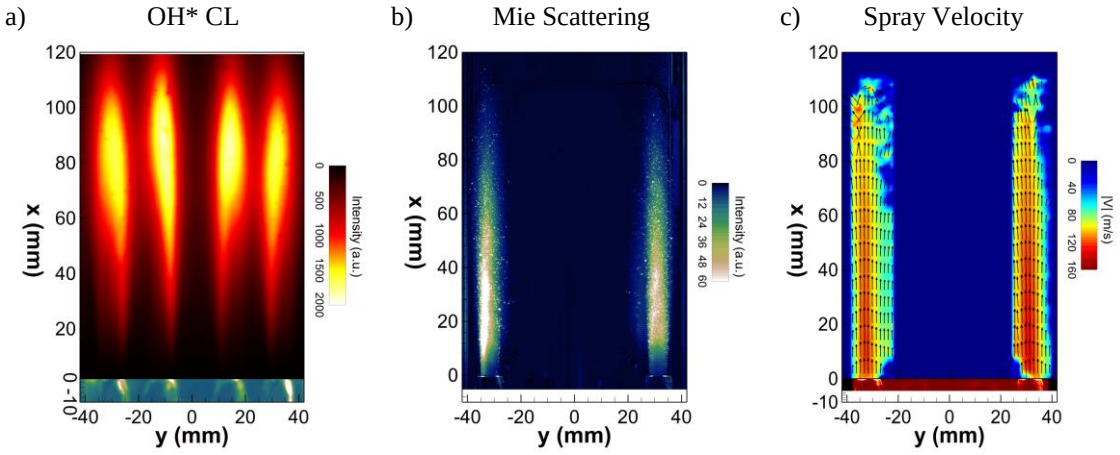

Figure 2. a) Mean OH* CL image, b) rms image of the Mie signal from spray particles exiting nozzles 5 and 8 and c) ensemble average of spray velocity measured in the flames of nozzle 5 and 8 of the test case.

Mie scattering images of the spray particles provide a good measure of the penetration depth of spray particles into the combustion chamber. The first frame of the spray particle image was used for determining the spray length. The average and rms images were calculated from 500 single shot images. The particle density and droplet size reduce (or decrease) along the x axis thus resulting in weak Mie signal in the mean image at downstream positions (not presented here), especially beyond x > 60 mm. This would give the impression of a shorter spray length even though there are spray particles surviving beyond x = 90 mm as seen in the rms images and will be confirmed later by the PDI results. Therefore the spatial distribution of the rms fluctuation in the measured Mie scattering signal was used as a more realistic marker for length or penetration depth of the spray. Figure 2 b) shows that the spray particles from nozzle 5 and 8 survive up to x = 100 mm and the distribution is similar even though the fuel plenums for the two nozzles are different.

The ensemble average of the spray velocity field shown in Fig. 2 c) was calculated from the spray particle images. The mean velocity field was obtained from 500 single shot velocity vector images. The ensemble velocity field presented in Fig. 2 c) represents the mean velocity of all droplets exiting from nozzles 5 and 8. The velocity magnitudes of the spray particles from both nozzles close to the nozzle exit are in good agreement with the v_{Jet} of the test case. The mean velocity field shows a slight decay of the velocity magnitude along the axial direction. The uniformity of the flame shape and length (Fig. 2 a), as well as the spray length and the velocity field from different nozzles confirm, that the fuel and air are evenly distributed between the 8 nozzles.

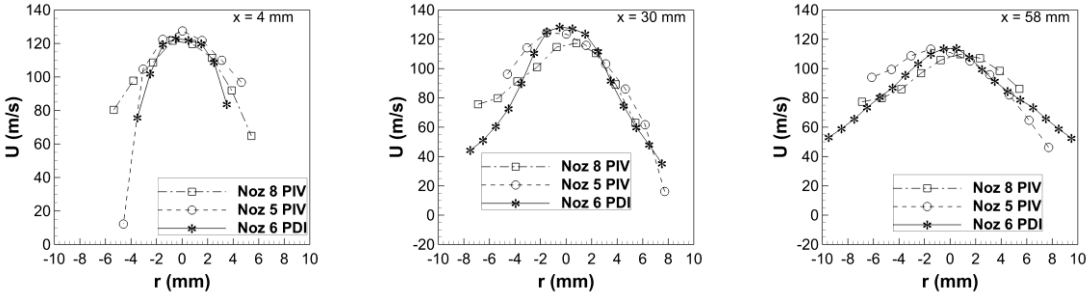

Figure 3. Comparison between the radial velocity profile extracted from mean velocity field measured using PIV technique over nozzles 5 and 8 and the mean velocity of all droplet sizes measured using PDI over nozzle 6 at axial locations x = 4, 30 and 58 mm respectively.

The homogeneous distribution is confirmed further by the comparison between the radial profile of the axial component (U) of the velocity obtained from PIV and PDI measurements. The radial profiles of mean U from three different axial locations, x = 4, 30 and 58 mm, measured over nozzles 5, 8 and 6 is presented in Fig. 3, where the former two nozzles have velocity from PIV measurement and the latter (nozzle #6) from PDI measurement. The PIV measurement is a planar measurement technique and in this case it provides 2D velocity field (3D velocity is possible with stereo PIV), but it does not discriminate the spray particle size and hence the measured velocity magnitude is the ensemble mean velocity of all droplets. The PDI is a point measurement technique where individual particle size and velocity are measured, therefore the velocity profile measured over nozzle 6 are the mean velocity of all droplets. The mean axial velocity profiles, at the three axial locations show good agreement of velocity magnitude between the three nozzles and the measurement techniques. The mean OH* CL image in Fig. 2a) and the mean axial velocity profile over three different nozzles being analogous confirms the symmetry of the burner.

B. Spray particles tracking gas phase

For PIV as well as PDI measurements in gaseous flows, the gas phase velocity is often tracked using 1 µm diameter seed particles of aluminum or titanium oxide. PIV measurements suffer significantly from window fouling when seed particles are introduced in the spray laden jets. The other major challenge is delineating the difference between signal from seed particles and liquid droplets where scattered signal form the larger liquid droplets is proportional to d^2. PDI measurement has a similar challenge where the receiver optics, the electronic hardware and software settings determine the droplet diameter size range that can be measured. Optimizing these settings for the seed particles will bias the measurements of spray droplets and vice versa. It has already been shown in a number of studies of jets laden with spray particles[29-32] that small droplets d <= 5µm follow the gas phase well and are good markers of the gas phase velocity. It is important to note that in all these studies either an ultrasonic nebulizer or an air assisted atomizer has been used for spray generation. Although the droplet distribution in all these studies are

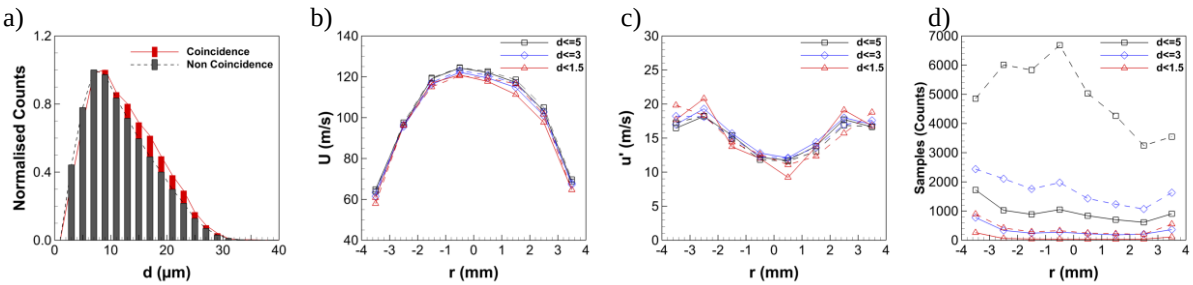

Figure 4. Comparison between coincidence (C - solid lines) and non-coincidence (NC - dashed lines) a) droplet distribution (measured at r = 0.5 mm), radial profiles of droplet b) mean and c) rms of axial velocity (U & u') and d) sample size for droplet bins d ≤ 5 µm (black lines), d ≤ 3 µm (blue lines) and d < 1.5 µm (red lines) at x = 4 mm.

comparable to technical applications, observed behavior of the small droplets (d ≤ 5 µm) cannot be directly transferred to the measurements presented in this paper where an industrial pressure atomizer is used, but it needs to be proved if droplets smaller than 5 µm can be used as tracers of the gas phase velocity.

In order to determine the response of the small droplets to turbulent fluctuations, the velocity profiles of the small droplets obtained from PDI measurements are compared. The PDI software was set to collect a sample of 10000 coincidence (C) measurements. A valid coincidence measurement is when the droplet size and the U and V component of the velocity of the same droplet are measured simultaneously. A byproduct of this is that all non-coincidence measurements are also saved. A non-coincidence (NC) measurement is where only the droplet size and U velocity component is measured, without a valid V velocity measurement, or when only the V component of the droplet velocity is measured without the size and U velocity component. The coincidence measurements are subject to low validation rates (higher rejection of data as all three parameters have not been measured simultaneously), which can lead to a significantly large number of non-coincidence measurements ($sample_{NC} = sample_{C} \times 10\text{-}20$) at a given sampling rate. The sample size of 10000 for the coincidence measurement was decided based on experience gained from previous measurements.

A comparison of the droplet size distribution measured at x = 4 mm and r = 0.5 mm, with droplet bin width of 2 µm, between coincidence (C - red solid line) and non-coincidence data (NC - dashed black line) are shown in Fig. 4 a). The NC data consists of measurements where droplet diameter and U velocity component were measured. Both droplet size distributions have been normalized by the largest sample of the plotted diameter bins. Almost negligible difference is observed in the shape of the droplet size distributions between the C and NC data, although there is a factor of 9 difference between the sample sizes. Hence a sample size of 10000 is enough for calculating mean values of the droplet size and the velocity for all droplets. Conditioning of droplet size and velocity to specific droplet bins may suffer from lack of samples, that is, the mean values have not converged. In combustion environment the life time of spray droplets reduces as the droplet diameter reduces and hence the average and rms values of the velocity is strongly influenced by the sample size of the respective droplet size bin. For this reason the axial velocity conditioned on three different droplet size bins from C and NC data are compared to eliminate data that may not have converged due to small sample size.

Radial profiles of the mean and rms of axial velocity (U & u′) of droplets in the size bin d < 1.5 µm, d ≤ 3 µm and d ≤ 5 µm, measured at x = 4 mm are presented in Fig. 4 b) and c). The velocity from C data is represented by solid lines and dashed lines represent the NC data. The velocity profiles of C and NC data in d ≤ 3 µm and d ≤ 5 µm bins overlap with each other and only a small difference is observed in the velocity magnitude between the two respective droplet bins. The velocity profile of droplets from NC data in the size bin d < 1.5 µm also overlaps well with all the other profiles. However the C data shows that the magnitude of the mean velocity of droplets in the size bin d < 1.5 µm is lower. The rms velocity profile of droplets in the size bin d < 1.5 µm also shows a more erratic behavior instead of a smooth profile, as observed for all the other diameter bins. This difference in the velocity profile of d < 1.5 µm from C data is due to the small sample size (less than 100 counts) as shown in Fig. 4 d). A minimum sample size of 200 is needed for a converged mean value. From the radial profiles of the sample sizes it can be seen that for samples larger than 200 counts, no difference in the velocity profiles are observed between the C and NC data for droplet bins d ≤ 3µm and d ≤ 5 µm. Spray particles in the droplet bin d < 1.5 µm are in the same size range as the aluminium or titanium oxide seed particles used in PIV and PDI measurements, therefore these spray particles will follow the gas phase. The similarity in the profile shape and magnitude of the mean and rms axial velocity of the different 3 droplet size ranges suggest that droplets smaller than 5 µm would be a good tracer for the gas phase velocity.

A better measure of how well the spray droplets in the size range d ≤ 5 μm respond to the turbulent fluctuations of the airflow is illustrated quantitatively via the Stokes number (*St*)[31]. The Stokes number (*St*) has been defined as the ratio of the droplet relaxation time τ_d to the turbulent time scale τ_t and is given in Eq. (4).

$$St = \tau_d/\tau_t \tag{4}$$

The definition of τ_d and τ_t are provided in Eq. (5) and Eq. (5) respectively;

$$\tau_d = \frac{4}{3}\frac{\rho_{liquid}}{\rho_{gas}}\frac{d}{C_D\langle|u_s|\rangle} \tag{5}$$

$$\tau_t = \frac{0.65R_{1/2\overline{u}}}{u'} \tag{6}$$

Where ρ is the fluid density, d is the droplet diameter, C_D is the droplet drag coefficient and u_s is the slip velocity between air and droplets. The equations for C_D used in this calculation can be found in Ref. 33. For the turbulence time scale calculation the large eddy length scale is defined here as the half radius of the gas phase velocity profile $R_{1/2\overline{u}}$ and u′ is the fluctuating axial velocity of the gas phase on the jet centerline. Spray droplets which follow the fluctuations of the gas phase have $St \ll 1$, while droplets that are unresponsive to any fluctuations have $St \gg 1$. Droplets with Stokes number close to unity have intermediate behavior where the droplets are partially responsive depending on the droplet size[31].

The axial profile of the Stokes number calculated for d ≤ 5 μm particles is presented in Fig. 5 for both coincidence and non-coincidence data. The gas phase mean and fluctuating velocities for the Stokes number calculation were obtained from the velocity profiles of droplets in the size bin d ≤ 3 μm. The Stokes number of the droplets in the size range d ≤ 5 μm ranges from 0.059 at x = 4 mm to 0.026 at x = 72 mm. The low Stokes number of d ≤ 5μm droplets concur that these droplets are able to follow the smallest turbulent scales and hence will be good tracers of the gas phase. The Stokes number calculated from C and NC data are also in good agreement, thus confirming that the sample size of 10000 for coincidence data is large enough, which was also seen in the velocity profiles presented in Fig. 4 b) and c). From here forth in this paper the gas phase velocity would be represented by velocity profiles of droplets in the size bin d ≤ 5μm and all droplet data are from coincidence measurements.

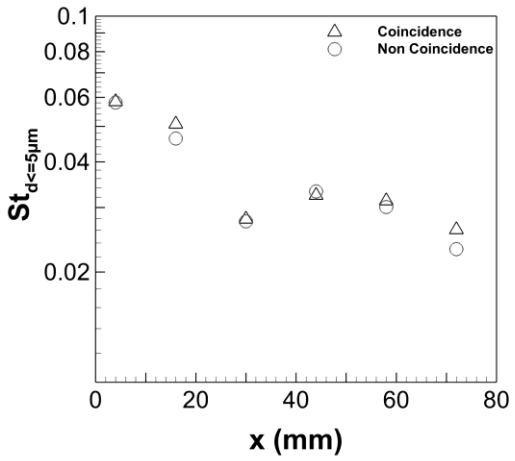

Figure 5. Axial profile of Stokes number of droplets d ≤ 5 μm from coincidence and non-coincidence data.

C. Droplet boundary condition at nozzle exit plane

The closest possible measurement location to the nozzle exit with the PDI system was x = 4 mm. Moving any closer to the nozzle exit resulted in clipping of one of the laser beams from the PDI transmitter. The radial scan of the measurements was done in the r direction across the nozzle as shown in Fig. 1. The changes in droplet size and velocity from the nozzle exit x = 0 mm to x = 4 mm is considered negligible and hence the measured droplet size and velocity profile at x = 4 mm is used to represent the boundary conditions at the nozzle exit plane. Figure 6 presents the radial profiles of mean and rms of a) axial (U & u′), b) transverse (V & v′) velocities and c) the droplet distribution and characteristic diameters (Dmn) measured at x = 4 mm. The velocity profiles in Fig. 6a) and 6b) consist of unconditioned velocities, i.e. from all droplets labeled as "All sizes", as well as conditioned velocities with respect to varying droplet size ranges. The droplet bins for the conditioned velocities are d ≤ 5, 5 < d ≤ 15, 15 < d ≤ 25 and 25 < d ≤ 35, where d is the droplet diameter in μm. Velocities of droplets larger than 35 μm have been left out due to sample size being less than 200 in this size group.

The mean axial (U) velocity across all droplet size ranges shows symmetric profiles similar to fully developed turbulent pipe flow. The gas phase (d ≤ 5 μm) velocity peaks at just over 120 m/s, which corresponds well with the

calculated v_{Jet}. The larger droplets (d > 5 µm) exiting the mixing tube are lagging behind the gas phase as shown in the mean U profiles in Fig. 6 a). The difference between the mean velocity of droplet (u_d) and gas phase (u_g) is defined as the slip velocity (u_s), i.e. $u_s = u_d - u_g$. The slip velocity of droplets in the size bins $5 < d \leq 15$, $15 < d \leq 25$ and $25 < d \leq 35$ are negative in the center of the jet with a transition to positive slip velocity beyond r = ±2 mm. The magnitude of u_s increases as the droplet diameter increases at the nozzle exit plane. The u′ profiles in Fig. 6 a) show higher fluctuations of the gas phase flow velocity compared to the velocities of the larger droplets exiting the nozzle. The u′ of the droplets decrease, as the droplet diameter increases. The velocity fluctuations of the gas phase increases from 9% at the jet centerline to 14% in the shear layer of the jet. Masri et al[34] have reported on so called wall effect which results in higher u′ of larger droplets in the shear layer. This effect is due to spray droplets hitting the wall and forming a thin film of liquid fuel which undergoes a secondary atomization at the exit plane. The u′ confirms that the nozzles of the liquid FLOX burner is not affected by this effect and this seems to be due to the thin air film feature that is part of the burner design.

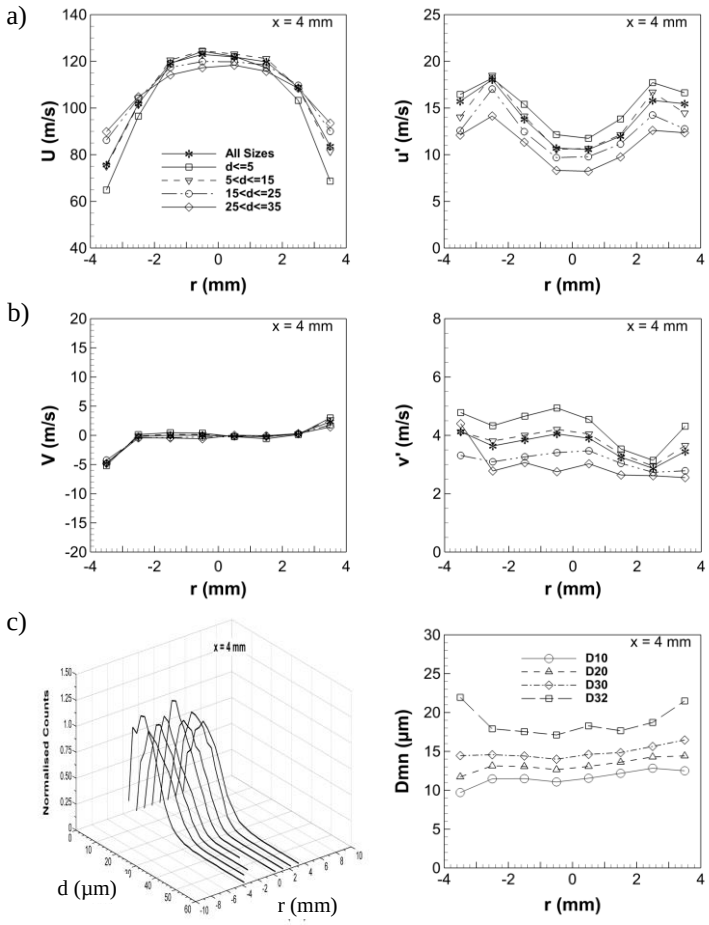

Figure 6. Radial profiles of mean and rms a) Axial (U), b) Transverse (V) component of droplet velocities and c) Droplet distribution and characteristic diameters (Dmn) measured at x = 4 mm. The droplet bins for the conditioned velocities are d ≤ 5 (Gas Phase), 5 < d ≤ 15, 15 < d ≤ 25 and 25 < d ≤ 35, where d is the droplet diameter in µm.

Figure 6 b) presents the radial profiles of mean and rms of the unconditioned and conditioned transverse velocity component (V & v′), measured across the nozzle at x = 4 mm. The mean transverse velocity V = 0 m/s, for all droplets in the central region of the jet confirms the symmetry of the jet at the exit plane. In the central region of the jet all droplets are transported axially with no radial movement. Close to the nozzle wall V increases which is due to the sudden expansion of the flow as it exits the mixing tube. The fluctuating component of the transverse velocity v′ shows a similar behavior as u′, that is the fluctuation of transverse velocity of the gas phase is higher compared to v′ of the larger droplets. The magnitude of v′ decreases with increasing droplet diameter, analogous to u′.

Figure 6 c) presents the droplet distribution measured radially across the nozzle at x = 4 mm. The bin width used for the droplet distribution plots is 2 µm and the droplet count in each bin has been normalized by the average of the maximum counts measured at r = -0.5 and 0.5 mm. Also presented in Fig. 6 c) are radial profiles of the characteristic diameters D10, D20, D30 and D32 respectively. The droplet distributions show that the majority of the droplets are in the size range 1 to 30µm and only a very small percentage of droplets are larger than 30µm in diameter. This is confirmed by the measured D32 of 18µm, which is also quite uniform across the central region of the nozzle. The peaks of the droplet distribution are also uniform across the nozzle exit. Due to very low validation rates (around 7% for C data) no reliable volume flux data could be obtained from the PDI measurements. The errors and challenges associated with flux measurements from PDI technique have been highlighted by Ferrand et al[30] for a well-planned and controlled lab experiment. The current experiment being performed at a test rig increases the complexity of obtaining accurate flux measurements. However, the droplet boundary conditions provided in Fig. 6 still provide valuable information for validation of CFD simulations, which will be presented in the section VII.

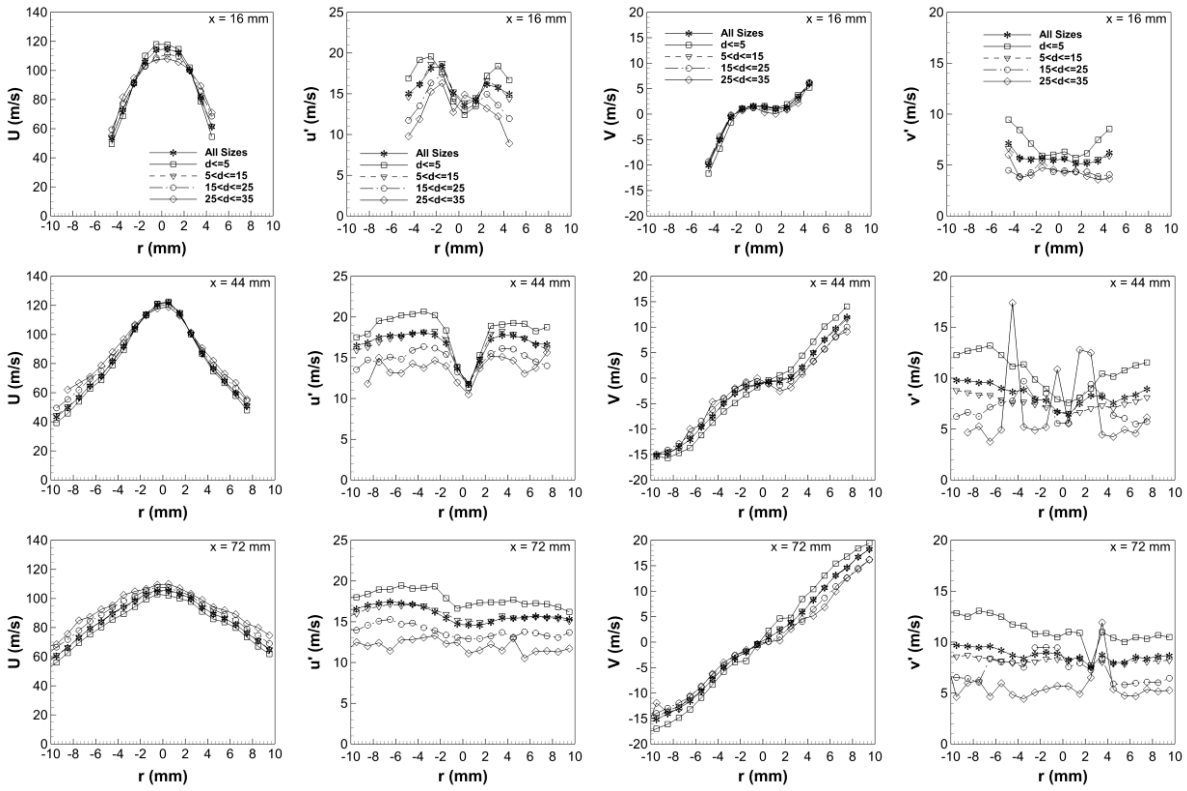

Figure 7. Radial profiles of mean and rms of the axial (U) and transverse (V) component of droplet velocities measured at x = 16, 44 and 72 mm. The droplet bins for the conditioned velocities are $d \leq 5$, $5 < d \leq 15$, $15 < d \leq 25$ and $25 < d \leq 35$, where d is the droplet diameter in µm.

D. Measured droplet field

Radial profiles of mean and rms of the axial (U) and transverse (V) velocity component, measured at 3 different downstream locations of 16, 44 and 72 mm are presented in Fig. 7. The velocity profiles in Fig. 7 consist of unconditioned velocity ('All Sizes') as well as conditional velocities (conditioned on droplet size, $d \leq 5$, $5 < d \leq 15$, $15 < d \leq 25$ and $25 < d \leq 35$), similar to the boundary conditions presented in Fig 6 a) and b). At x = 16 mm the gas phase velocity is higher than the velocities of droplets larger than 5 µm, i.e. the u_s of droplets in the size bins $5 < d \leq 15$, $15 < d \leq 25$ and $25 < d \leq 35$ µm are still negative in the jet core. Close to the shear layer region (r > 2 mm) it can be seen that all droplets larger than 5µm have transitioned to positive u_s. Further downstream at x = 44 mm the u_s of the larger droplets are almost zero or slightly negative only close to the central axis of the jet. At x = 78 mm all large droplets lead the gas phase velocity, i.e. all large droplets have positive u_s. It can be seen from the profiles of mean U in Fig. 6 a) and Fig. 7 that the decay of the centerline gas phase velocity along the x axis is faster compared to the mean U of the larger droplets. Although the large droplets exit the mixing tube slower than the gas phase, the deceleration of the droplet U is much slower compared to the gas phase velocity.

The radial profiles of u′ at x = 16 mm have similar shape to the profiles observed at x = 4 mm but the magnitude of the fluctuations of the gas phase and large droplets are swapped, close to the jet centerline where the u′ of the gas phase is lower than u′ of the large droplets. In the shear region the fluctuations in the gas phase velocity is higher than the droplets and u′ decreases as the droplet diameter increases. Further downstream at x = 44 mm the u′ close to the centerline goes back to the trend observed at x = 4 mm, and as one moves radially outwards the magnitude of u′ increases to a maximum and then remains almost constant. The intensity of the gas phase velocity fluctuation is still higher than the u′ of larger droplets which also decreases as droplet diameter increases. At x = 72 mm the u′ of the gas phase and the droplets are uniform right across the jet with the gas phase velocity fluctuations still higher than the u′ of large droplets.

The radial profiles of the transverse velocity (V) presented in Fig. 7 confirm the symmetry of the spray jet. The spreading rate of the gas phase and the large droplets is same at x = 16 mm with the central region of the vapor and

droplet field having zero momentum in the transverse direction. Moving further downstream from x = 30 to 72 mm the magnitude of V gradually increases when moving radially outwards. It can be seen that the spreading rate of the gas phase is now faster than the spreading rate of the larger droplets at both of these axial locations. The v′ of the gas phase and droplets in the size bins $5 < d \leq 15$, $15 < d \leq 25$ and $25 < d \leq 35$ increases as one moves downstream from the nozzle exit plane. The v′ of the gas phase is always higher than the v′ of the larger droplets, and as the droplet diameter increases the fluctuations in the transverse velocity of the corresponding droplets decrease.

Figure 8 presents the droplet distribution measured radially across the nozzle and radial profiles of the characteristic diameters D10, D20, D30 and D32 at x = 16, 44 and 72 mm respectively. The bin size used for the droplet distribution plots is 2 µm and the droplet count in each bin has been normalized by the average of the maximum counts measured at r = -0.5 and 0.5 mm. The droplet size distribution shows that the majority of the droplets are in the size range 1 to 30 µm at all axial locations from x = 16 to 72 mm. The droplet distributions are quite uniform right across the jet and significant difference is observed only at the edge of the jet. Very small changes are observed in the magnitude of the characteristic diameters D10 to D32, from x = 16 to 72 mm. It has already been shown in Fig. 7 that the mean axial velocity of the larger droplets does not decrease significantly between x = 16 to 72 mm. This also explains the long flame and spray lengths observed in Fig. 2 a) and b). A detailed set of experimental spray data from measurements performed in the liquid FLOX® burner is now made available to validate the CFD simulation of the test flame case and this is presented the next section.

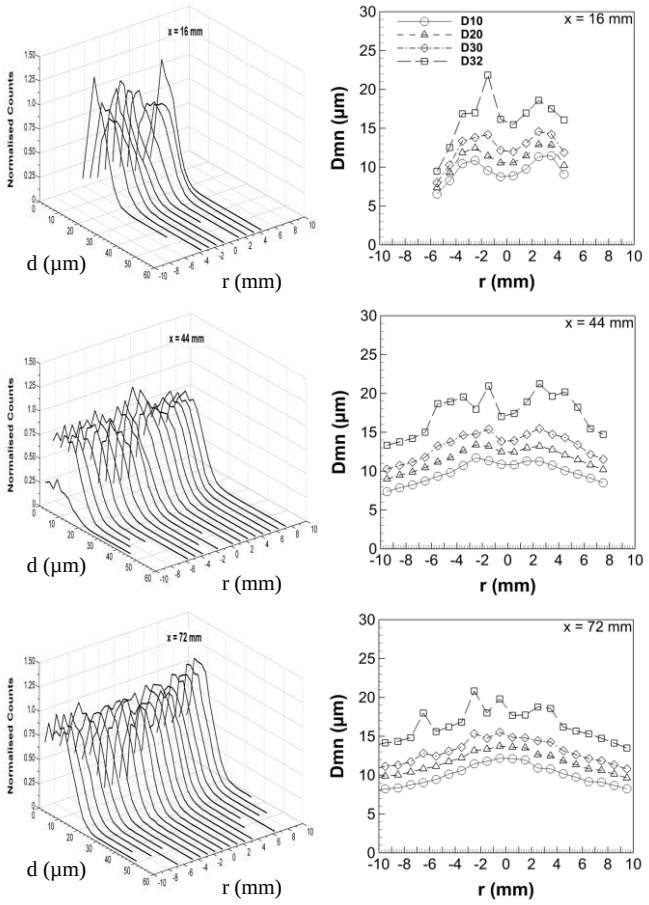

Figure 8. Radial profiles of droplet distribution and characteristic diameters (Dmn) measured at x = 16, 44 and 72 mm.

VII. Numerical Simulation Results

The injector used in this study is a pressure atomizer which is mounted 139 mm upstream of the nozzle exit plane. An estimation of the SMD produced by such atomizers, from empirical relations[35], resulted in a SMD of 92 µm. The large aerodynamic Weber number (>1000) indicated that secondary droplet breakup does occur after the primary breakup. Employing the CAB secondary breakup model of Tanner[36] in the simulation showed that secondary breakup is completed inside the mixing chamber (section upstream of the mixing tube inlet). Exploratory changing model parameters influencing the secondary atomization yielded quite different results for the normalized liquid mass flow and the characteristic spray diameters at the exit of the mixing pipe. Therefore the use of a secondary breakup model for the present study was abandoned and the spray from the injection nozzle as a root normal size distribution with an SMD = 19.5 µm and a width of MMD/SMD = 1.10 was used, the latter being a width inside the typical range for atomizers in gas turbines[37]. With these choices the measured size distribution and its characteristic diameters at x = 4 mm were matched quite well.

In the investigated test case the incoming total air flow is split into air for the 8 nozzles and a small fraction for impingement cooling of the burner front plate. The cooling air was then fed into the combustion chamber by a circumferential slot, see Fig. 15 b). The fraction of total air used for the cooling was not measured in the experiments, however it could be determined from the simulation to be 0.164. This was achieved by adjusting the air

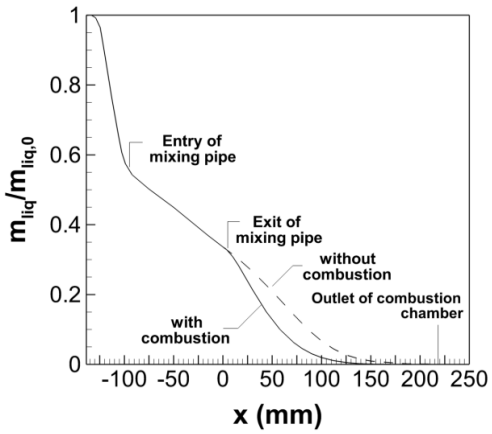

Figure 9. Evolution of the calculated liquid mass flow normalized by the injected mass flow for "cold" (dashed line) and "hot" (solid line) simulations.

inflow into the plenum for the simulated nozzle, such that the calculated maximum of the axial velocity profile of small droplets at x = 4 mm for the "cold" simulation (without combustion) met the "hot" (with combustion) measured values of ~122 m/s (d ≤ 5 µm, Fig. 6 a). This procedure is justified, because a) the hot experiment showed, that at x = 4 mm the gas jet flow was still cold, as the lift-off height of the flame observed in the experiment was further downstream, roughly in the range x = 15-20 mm, b) the cold simulation showed that the maximum of the axial velocity profile of gas and small droplets from the cold simulation at x = 4 mm and x = 0 mm have nearly the same value.

In the course of the numerical simulations, the 1-step global EDM/FRC model was initially applied to the whole computational domain. It predicted a very fast onset of the heat release, already in the mixing tube, whereas the measurements showed that the burning starts inside the combustion chamber as it should. In order to overcome this early onset of the predicted heat release, the simulation was split into two parts: First a "cold" computation without combustion for the whole computational domain was performed. Then we extracted both the computed gas field solution and the spray profiles obtained at the end of the mixing tube (x = 0) and used it as the inlet conditions for a successive "hot" simulation of the reacting flow only in the combustion chamber. This moved the onset of the heat release into the combustion chamber. The onset of the heat release was still quite early, but it was good enough to enable a meaningful comparison of the calculated and measured spray quantities.

The calculated stream wise development of the liquid mass flow normalized by the initial (injected) liquid mass flow is a measure for the evaporation progress of the spray. Figure 9 shows the evaporation progress from the simulations with and without combustion, starting from the injector until the outlet of the combustion chamber. It shows already a fast evaporation in the mixing chamber just before the inlet of the mixing tube, due to the inlet air temperature of 573 K. The subsequent reduction in evaporation rate in the mixing tube is caused by the reduced residence time of the evaporating parcels due to the much higher gas velocity in the pipe. After the exit (x = 0) of the mixing tube the normalized liquid mass flow has already decreased to 0.336 , i.e. 2/3 of the initial liquid mass has already been evaporated in the nozzle (mixing chamber & mixing tube). It should be mentioned here that this value was obtained on the assumption of an instantaneous secondary breakup after the injection nozzle. (For comparison: The use of the secondary breakup model with different model parameters had given significantly lower values in the range 0.05-0.16, i.e. a still faster evaporation progress). It can be seen from Fig. 9 for the cold simulation in the combustion chamber, that the evaporation rate is enhanced again due to the lower gas velocity level (causing longer travel times of the particles to reach an axial position) in the combustion chamber compared to the mixing pipe. Moreover Fig. 9 shows a strong enhancement of the evaporation due to the combustion. From Fig. 2 b) the particles could be observed in the experiment up to x = 100-120 mm. This is confirmed by Fig. 9, where the normalized

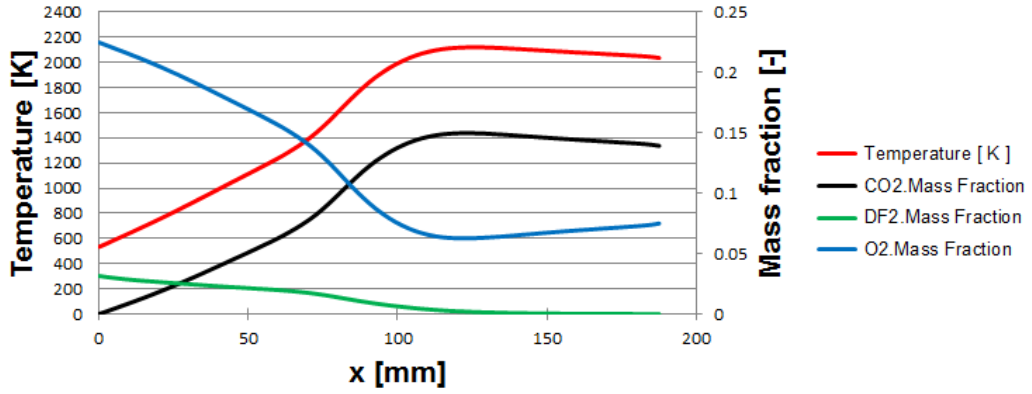

Figure 10. Evolution of calculated gas temperature and species mass fractions along the centerline of nozzle #6.

liquid mass flow at x = 100, 120 and 150 mm of the simulation is down to 0.0196, 0.0073 and 0.0008, respectively, and all all spray particles were evaporated before reaching the outlet as shown later in the plot of particle trajectories in Fig. 15 c).

Figure 10 shows the computed evolution of gas temperature and CO_2, O_2 and H_2O mass fractions in the combustion chamber along the centerline of the simulated nozzle (#6). It can be seen, that in the simulation there is already at x = 4 mm a gas temperature rise due to the early onset of reaction. This rise in gas temperature in turn locally raises (via the lowering of the gas density) the maximum axial jet velocity compared to the measurement, as the radial expansion of the jet into the chamber happens slower than the simulated heat release. As the nozzle axis is not the combustion chamber axis, the gas jet center begins to leave the centerline of the mixing tube. This happens far downstream and is the reason for the slight decrease of the eventual gas temperature and mass fractions of CO_2 and H_2O beginning at x~120 mm. It should be mentioned here, that the final adiabatic gas temperature and final gas composition of the 1-step reaction model was verified by the values obtained from the gas equilibrium code Gaseq[38].

Computational spray results were obtained from spray parcel data at the registration planes designated at respective axial locations. The PDI-measurements were done along a full radial traverse across the nozzle axis at different axial locations. Nevertheless, in the numerical simulation it was advantageous, to use a cylindrical registration grid on the registration planes covering the full cross section, where the spray was located, to capture the data during the Lagrangian particle tracking. As in the case of the measured profiles, the simulations also showed, until the last axial measurement position x = 72 mm that the flow was still axisymmetric to the nozzle axis.

Figure 11 shows radial profiles of the calculated liquid volume flux distribution at different axial locations in the combustion chamber. At the beginning of the mixing pipe (x = −92 mm, not shown in the figure) the radial profile of the liquid volume flux of the droplets has a maximum at the pipe center and an additional bump at r = 1.4 mm. In the course of the further downstream development of that profile in the pipe, both maxima become lower and the bump moves toward the pipe wall. Fig. 11 shows, that finally at the exit of the mixing pipe (x = 0) most of the spray has concentrated near the pipe wall (r = 3.5 mm). The underlying radial movement of particles in the pipe from the region of high axial velocity to low axial velocity is an effect of the turbulent particle dispersion in the shear flow of the pipe. As that radial particle drift is limited by the pipe wall, the particles accumulate there. Downstream (x > 0) of the pipe exit the bounding pipe walls are no longer present, and the droplets spread radially into the chamber. So the accumulated maximum of the liquid volume flux profile near the radius of the pipe wall reduces (x = 10 mm) and finally disappears at x = 72 mm. This spreading of the particles is larger than the spreading of the gas jet (cf. the axial velocity of the large particles compared to the gas in Fig. 12 at x = 72 mm) according to the particle inertia (particle's Stokes number). It should be noted here, that volume flux profiles from the PDI measurements in the combustion chamber exist. However they are not calibrated and cannot be used for any quantitative comparisons. Nevertheless they confirm the presence of accumulated liquid volume near the wall of the pipe

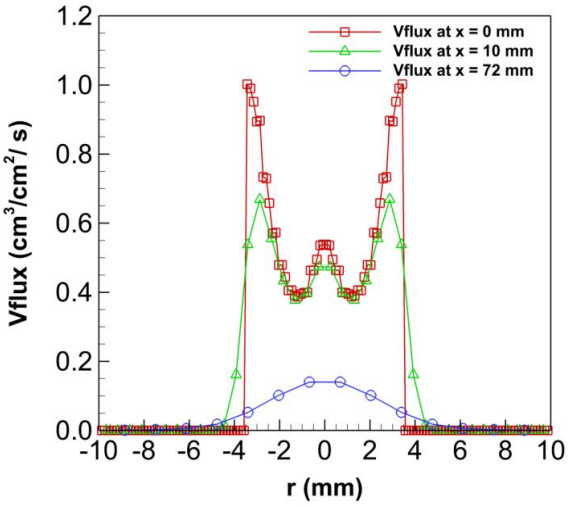

Figure 11. Calculated radial profiles of liquid volume flux at three different axial locations.

Figure 12 presents the comparison between the calculated and measured radial profiles of the mean and rms of axial and radial velocities at different axial locations. From the axial velocity plots it can be seen that the mean axial gas velocity peaks just over 120 m/s which is close to v_{Jet}. At x = 4 mm, the mean axial velocity at the centerline has a velocity of 125.0 m/s which is slightly higher than the measured value. This is due to the early heat release predicted by the combustion model and the slow radial expansion of the jet predicted by the turbulence model. At x = 4 mm, droplets in the size class 15 < d ≤ 25 µm are lagging behind the gas phase indicating negative slip velocity in the jet core as shown in Fig. 12. These large droplets attain positive slip velocity beyond r = ±3.5 mm when compared to r = ±2 mm as observed by measurements. At x = 16 mm, in the jet core the particles in the size class 15 < d ≤ 25 µm, still have negative slip velocity, but transition to positive slip velocity beyond r > 3.5 mm. Further downstream at x = 72 mm all particles have transitioned to positive slip velocity in the jet core similar to the observations made in the experiments. At increasing downstream distance the simulated mean axial velocities have

higher values close to the centerline than measured values and this is due to slower spreading of the jet. The decay of the centerline velocity in the simulations is slower than the measurements with increasing downstream distance. High velocity at the centerline could be due to the turbulence model used, which underpredicts the gas turbulence intensity.

From the calculated rms axial velocities presented in Fig. 12, it can be observed that at x = 4 mm the gas phase axial rms velocity in the jet core is higher than for the largest diameter particles. But the magnitude of u' for all axial locations is less then measured. Moreover, experimental u' at x = 72 mm is nearly constant across the jet, but in the numerical simulation this characteristic is observed only at x = 120 mm (not shown here) confirming inaccuracy of the turbulence model in predicting the spreading of the gas jet.

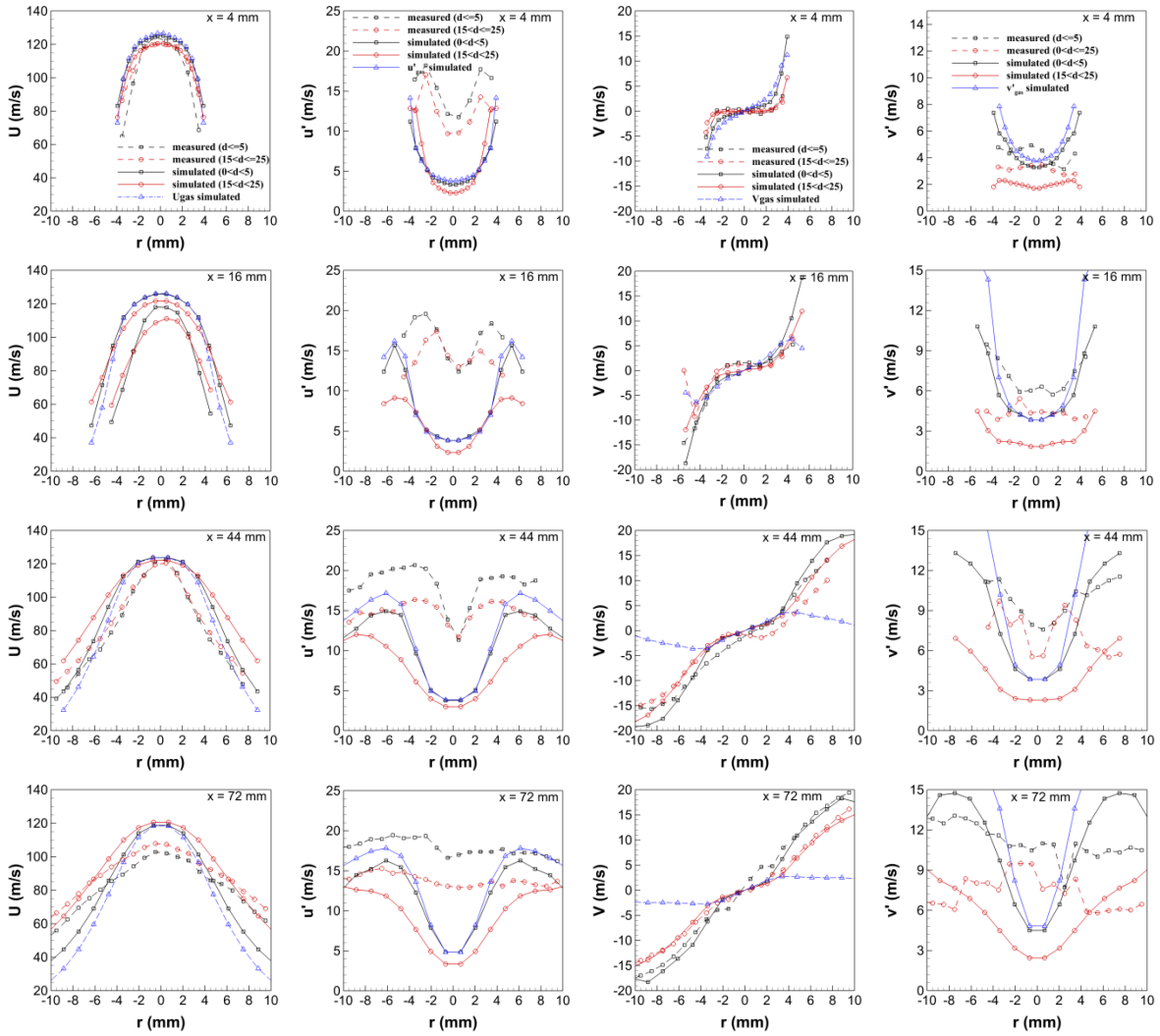

Figure 12. Comparison of calculated (solid lines) and measured (dashed lines) radial profiles of mean and rms of the axial (U & u′) and radial (V & v′) velocities of droplets in the size bins d ≤ 5 µm (black lines) and 15 < d ≤ 25 µm (red lines) at four different axial locations. Radial profiles of mean and rms of the axial and radial velocities of the gas phase from simulation is represented by the blue line.

Figure 12 also shows the calculated and measured radial profiles of the mean and rms radial velocities. For all axial locations the magnitude of the calculated mean radial particle velocity increases gradually when moving radially outwards and a good agreement is obtained between the calculated and the experimental findings. The simulation shows that for r > 2 mm, even the mean radial velocity of the small particles supercedes the mean gas radial velocity. This is due to the inertia of the particles. With regards to radial fluctuation velocity, the calculated

gas phase v' is higher than the v' of large diameter particles and v' decreaseas with increaseing particle diameter as confirmed by the experiment. So we can state, that the shape of the calculated radial profiles of axial and radial fluctuation (rms) velocities are captured properly, but the level of the values tends to be too low especially in the inner radial region of the gas jet. This is due to the computed low level of gas turbulence intensity (turbulent kinetic energy) there.

The calculated and measured radial profiles of the characteristic spray diameters at different axial locations are presented in Fig. 13. As mentioned earlier, a SMD of 19.5 µm was employed at the injection nozzle (x = -139 mm) during cold simulation (without combustion). For the hot simulation (with combustion) a single size distribution for the particles starting from all radial locations in plane x = 0 was obtained from the cold simulation there, as the radial profiles of the characteristic diameters obtained from the measurements at x= 4 mm were nearly constant. That is why at x = 4 mm the calculated characteristic diameters in Fig. 13 are still nearly constant across the jet. The plots in Fig. 13 show that the radial profiles of the characteristic diameters capture well the shape of the measured profiles. Also the width (defined as the ratio of SMD/D10) of the measured size distribution is met. The calculated characteristic diameters rise with increasing axial distance, whereas the measured characteristic diameters remain almost constant with axial distance.

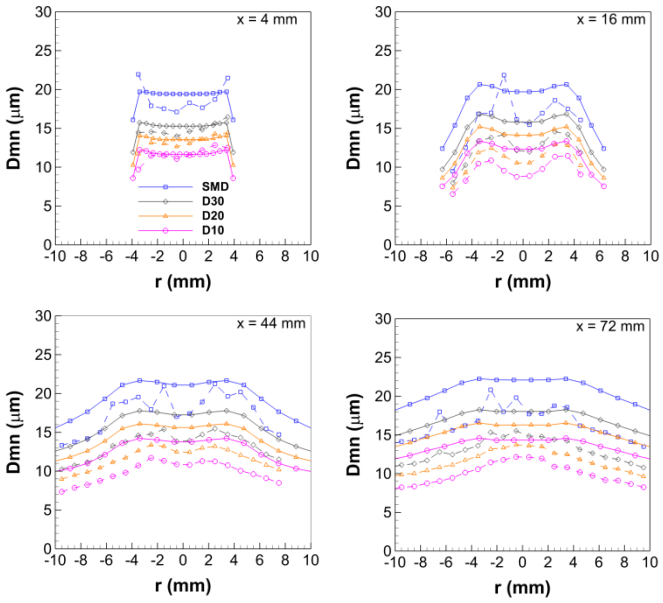

Figure 13. Comparison of calculated (solid lines) and measured (dashed lines) radial profiles of characteristic spray diameters at different axial locations.

Although the evaporation of an individual droplet in a spray always decreases its diameter, the evaporation of a spray can lead to a temporary increase, decrease or maintain nearly constant characteristic diameters of the spray. This behavior of the characteristic diameters in the course of the evaporation is not an indicator for a slow or fast evaporation. Evaporation on one hand leads to a removal of small droplets from the spray (this tends to raise the characteristic diameters, e.g. the SMD) but on the other hand to a reduction of larger droplets to medium size droplets (this tends to decrease the characteristic diameters). So there is a dynamic filling and depleting of the bins of the size distribution of an evaporating spray. The actual change of the characteristic diameters due to evaporation depends on the initial shape of the size distribution and the gasfield experienced by the individual particles of the spray. Only in a very late state of the evaporation of a spray the characteristic diameters converge, then collapse into 1 line and end up at a value of zero.

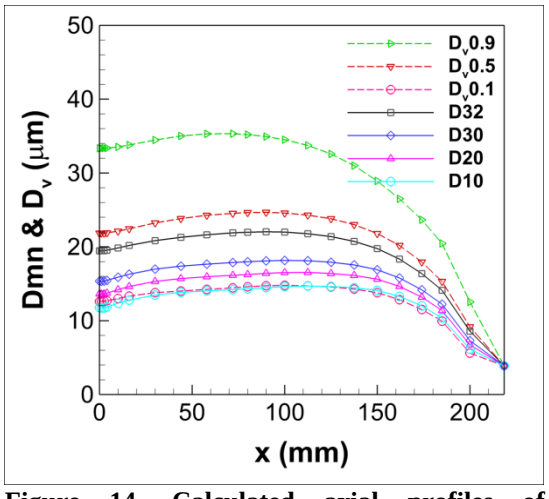

Figure 14. Calculated axial profiles of characteristic spray diameters.

This can be clearly seen in Fig. 14. It shows the evolution of different characteristic diameters including some volume undersize diameters ($D_v0.1$, $D_v0.5$, $D_v0.9$) along the axial distance for the hot simulation. In each axial registration plane, the characteristic diameters were calculated from all particles that passed the plane. It can be observed from Fig. 14, that the characteristic diameters increase until around x = 120 mm (this rise was already mentioned in the radial profiles of Fig. 13) even though strong evaporation is present (cf. Fig. 9) and this increase is due to the above mentioned reasoning. Beyond x = 120 mm, where only a tiny fraction of the initial liquid spray volume is still present, all characteristic diameters fall continuously and converge. All characteristic diameters meet at a single value, namely the diameter of the very last particle at the moment, where the penultimate particle (in

a)

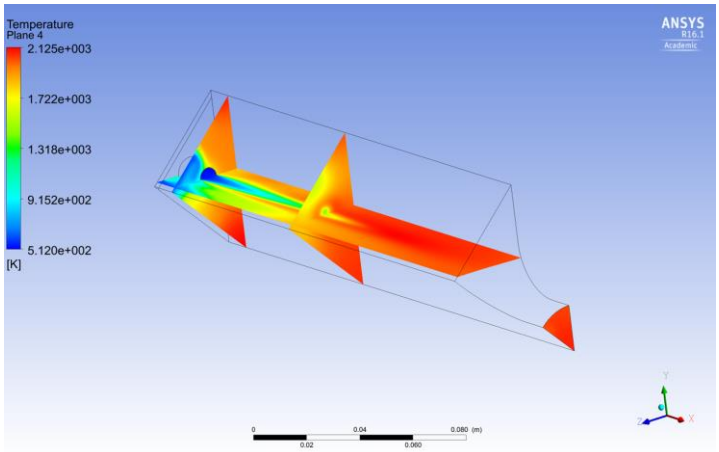

b)

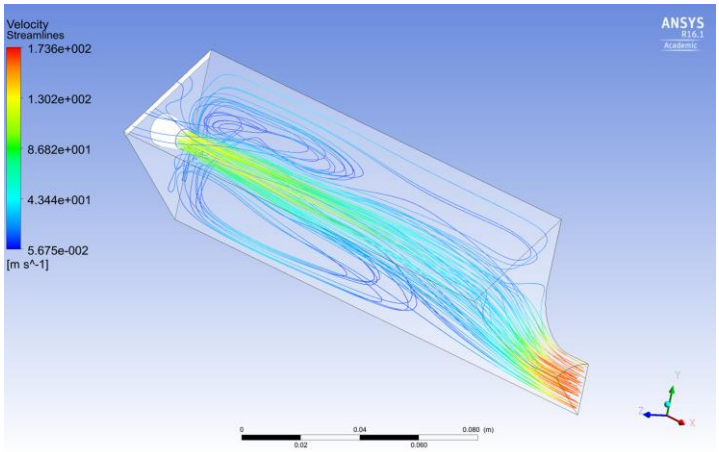

c)

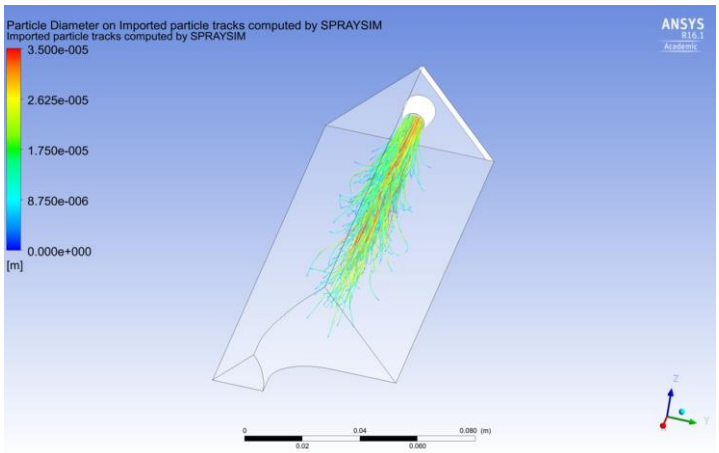

Figure 15. a) Computed gas temperature field in selected planes of the combustion chamber. b) Computed streamlines in the combustion chamber. c) Particle trajectories computed by SPRAYSIM. (Note: y and z axes are interchanged in Fig. 15 compared to Fig. 1 b)

our case of 2 million of started computational particles) is just evaporated. This happend just before the outlet. Hence the course shown in Fig. 14 demonstrates complete evaporation in accordance with Fig. 9. The fact, that the measured characteristic diameters in Fig. 13 remained roughly constant in measured planes x = 4 to 72 mm, whereas the computed values rose there, is simply the result of a somewhat different initial size distribution at x = 0 interacting with a different gasfields, especially the gas temperature field. Once again, the combustion model is of strong influence. (It should be mentioned here, that in the simulation without combustion the axial development of

the SMD was nearly constant from the injection nozzle to the exit of mixing pipe even though strong evaporation was already present there, see Fig. 9).

Figure 15 a) shows the calculated temperature field in selected planes in the combustion chamber. The xz- plane shows the gas jet. In the near field of the nozzle, the reaction zone is around the gas jet, whereas the jet core still remains relatively cold. As a consequence, the shown radial temperature profile does not uniquely define the flame lift-off height. The yz- plane close to the nozzle shows a distinct blue zone which is caused by the feeding of impingement cooling air through the axial slot into the combustion chamber. In the outlet cross section it is observed that the temperature is not fully uniform throughout the area: the maximum temperature at the outlet plane (x = 218.5 mm) is found to be 2084 K close to the geometric axis of the combustion chamber and minimmum temperature of 2025 K away from the geometric axis of combustion chamber. The CO_2 distribution in the outlet when normalized by its max. and min. values (0.1461 and 0.1390, resp.) exhibits nearly the same pattern as the normalized temperature distribution, so the CO_2 mass fraction in the outlet is higher, where the temperature is higher. These maximum and minimum CO_2 mass fractions are in close agreement with the equilibrium value of 0.1439 predicted by Gaseq[38] for the combustion of the light heating oil with λ_G of 1.45. Further, the ratio of the computed mass flow of CO_2 through the outlet to the theoretical mass flow of CO_2 produced for complete combustion of the fuel is 0.99938. This indicates that the 1-step reaction is fully completed inside the combustion chamber.

Figure 15 b) shows some streamlines in the combustion chamber. Existence of three distinct recirculation zones is visible. The two recirculation zones are present above and below the nozzle axis and help in stabilization of the flame. The third recirculation zone is located at the exhaust wall of the combustion chamber. It is rather weak and due to the flow bending from the nozzle axis to the outlet. Also visible are streamlines which emanate from the axial slot tangentially into the combustion chamber which are later entrained into the recirculating flow.

Figure 15 c) shows particle trajectories computed by SPRAYSIM. 500 trajectories are shown in the figure. They reveal that the spray jet is actually symmetric in the measured axial range (x < 72 mm). The effect of the turbulent dispersion model is clearly visible. Finally, none of the spray particles reach the outlet indicating that complete evaporation of the spray occurs.

VIII. Conclusion

Spray characteristics in a liquid fuel combustor based on the FLOX® burner concept has been investigated at the HIPOT rig at the DLR Institute of Combustion Technology. A stable flame of BOP at a pressure, preheat temperature, λ_G, and v_{Jet} of 3.5 bars, 300 °C, 1.45 and 120 m/s respectively, was chosen as the test case for detailed measurement and numerical analysis of the spray characteristics. Mean flame shape from OH* CL image showed long flame length with a short flame lift off height. The measured spray length showed large penetration depth of the spray into the combustion chamber from the nozzle exit plane, since spray droplets are still present downstream of the peak heat release region. The droplet velocity field show large droplets (d > 15 µm) attaining positive slip velocity beyond x = 44 mm downstream of the nozzle exit plane. A comprehensive data set with detailed spray characteristics was made available for CFD simulations in order to better understand the evaporation process taking place in the flames of the liquid FLOX® burner.

The calculated and measured spray behavior in the combustion chamber showed satisfying agreement. The results from the simulations showed that a large portion of the evaporation happened already in the nozzle, although future investigation will be required to quantify the influence of the secondary breakup on the evaporation in the nozzle. Even though intense evaporation is predicted in the combustion chamber where the spray was fully evaporated, spray particles still penetrate deep into the combustion chamber (x > 150 mm). Some differences were observed in the droplet axial and radial velocity profiles between simulation and measurements due to the low turbulence intensity prediction and slow spreading of the gas jet in the combustion chamber computed by the SST two-equation turbulence model. However this will be addressed in the future CFD work where a better turbulence model such as LES, VLES, MILES could be applied, for which SPRAYSIM can be also applied. The simulation showed that the spray fully evaporated inside the combustion chamber and the spray characteristics was mainly affected due to the simple global 1-step combustion model with simple turbulence-chemistry interaction model EDM/FRC, which predicted a too early onset of the heat release. The use of a detailed finite rate chemistry model and turbulence-chemistry interaction model is a must for a quantitatively good prediction (not post-diction) of the two-phase flow in the combustion chamber. Overall, the experimental and computational results complemented each other, and both together provided a much better insight into the behavior of the spray flame for further development of the liquid FLOX® burner.

The future outlook for continuing development of the burner involves reducing the flame length. This will require further improvement for of the numerical codes as well as physical changes to the burner geometry. Custom designed atomizer for this application as well as changes to the combustion chamber will also be considered. Other areas of focus would be to improve flow pattern around the injector and consider MGT efficiency improvement via recuperation (higher preheat temperatures) while avoiding coking.

Acknowledgments

The authors would like to thank Mr. Jochen Eichhorn and Dr. Peter Kutne, for their assistance with test rig operation, design and manufacturing of the burner.

References

[1]Lückerath, R., Meier, W. and Aigner, M. "FLOX® Combustion at High Pressure With Different Fuel Compositions," *Journal of Engineering for Gas Turbines and Power*, Vol 130, No. 1, 2008, pp. 011505-011505.
[2]Schütz, H., Lammel, O., Schmitz, G., Rödiger, T. and Aigner, M. "EZEE®: A High Power Density Modulating FLOX® Combustor ", Copenhagen, Denmark, 2012, June 11-15, pp. GT2012-68997.
[3]Schütz, H., Lückerath, R., Kretschmer, T., Noll, B. and Aigner, M. "Analysis of the Pollutant Formation in the FLOX® Combustion," *Journal of Engineering for Gas Turbines and Power*, Vol 130, No. 1, 2008, pp. 011503-011503.
[4]Schütz, H., Lückerath, R., Noll, B. and Aigner, M. "Complex Chemistry Simulation of FLOX®: Flameless Oxidiation Combustion," *Clean Air International Journal of Energy Clean Environment*, Vol 8, No. 3, 2007, pp. 239ff.
[5]FLOX® is a registered trademark of WS Wärmeprozesstechnik GmbH, Renningen, Germany.
[6]Wünning, J. A. and Wünning, J. G. "Burners for Flameless Oxidation with Low NOx Formation even at Maximum Air Preheat," Vol 41, No. 10, 1992, pp. 438-444.
[7]Wünning, J. A. and Wünning, J. G. "Flameless oxidation to reduce thermal no-formation," *Progress in Energy and Combustion Science*, Vol 23, No. 1, 1997, pp. 81-94.
[8]Bobba, M. K., Gopalakrishnan, P., Seitzman, J. M. and Zinn, B. T. "Characteristics of Combustion Processes in a Stagnation Point Reverse Flow Combustor", Barcelona, Spain, 2006, May 8-11, pp. GT2006-91217.
[9]Coelho, P. J. and Peters, N. "Numerical simulation of a mild combustion burner," Vol 124, No. 3, 2001, pp. 503-518.
[10]Weber, R., Verlaan, A., Orsino, S. and Lallemant, N. "On Emerging Furnace Design Methodology that Provides Substantial Energy Savings and Drastic Reductions in CO2, CO and NOx Emissions," *Journal of the Energy Institute*, Vol 72, No. 1999, pp. 77-83.
[11]Lammel, O., Schütz, H., Schmitz, G., Lückerath, R., Stöhr, M., Noll, B., et al. "FLOX® Combustion at High Power Density and High Flame Temperatures," *Journal of Engineering for Gas Turbines and Power*, Vol 132, No. 12, 2010, pp. 121503-121503.
[12]Roediger, T., Lammel, O., Aigner, M., Beck, C. and Krebs, W. "Part-Load Operation of a Piloted FLOX® Combustion System," *Journal of Engineering for Gas Turbines and Power*, Vol 135, No. 3, 2013, pp. 031503-031503.
[13]Lammel, O., Rödiger, T., Stöhr, M., Ax, H., Kutne, P., Severin, M., et al. "Investigation of Flame Stabilization in a High-Pressure Multi-Jet Combustor by Laser Measurement Techniques", *Proceedings of ASME Turbo Expo*, Düsseldorf, Germany, 2014, June 16-20, pp. GT2014-26376.
[14]Seliger, H., Huber, A. and Aigner, M. "Experimental Investigation of a FLOX®-Based Combustor for a Small-Scale Gas Turbine Based CHP System under Atmospheric Conditions", *Proceedings of ASME Turbo Expo*, Montreal, Quebec, Canada, 2015, June 15–19, pp. GT2015-43094.
[15]Zanger, J., Monz, T. and Aigner, M.,Experimental Investigation of the Influence of Combustor Cooling on the Characteristics of a FLOX®-Based Micro Gas Turbine Combustor edited by Benini, E., *Progress in Gas Turbine Performance*, InTech 2013. pp. 165–184.
[16]Zanger, J., Monz, T. and Aigner, M. "Experimental Investigation of the Combustion Characteristics of a Double-Staged FLOX®-Based Combustor on an Atmospheric and a Micro Gas Turbine Test Rig", *Proceedings of ASME Turbo Expo*, Montreal, Quebec, Canada, 2015, June 15–19, pp. GT2015-42313.
[17]Zizin, A., Lammel, O., Severin, M., Ax, H. and Aigner, M. "Development of a Jet-Stabilized Low-Emission Combustor for Liquid Fuels", *Proceedings of ASME Turbo Expo*, Montreal, Quebec, Canada, 2015, June 15–19, pp. GT2015-42642.

[18]Gounder, J. D., Zizin, A., Lammel, O. and Aigner, M. "Spray characteristics measured in a new FLOX® based low emission combustor for liquid fuels using laser and optical diagnostics", *Proceedings of ASME Turbo Expo*, Seoul, South Korea, 2016, June 13–17, pp. GT2016-56629.
[19]Boyde, J. M., Clercq, P. L., Domenico, M. D., Rachner, M., Gebel, C. G., Mosbach, T., et al. "Validation of an ignition and flame propagation model for multiphase flows", *Proceedings of ASME Turbo Expo*, Vancouver, Canada., 2011, June 6-10, pp. GT2011-45104.
[20]Eckel, G., Grohmann, J., Rachner, M., Le Clercq, P. and Aigner, M. "LES of a generic swirl-stabilized spray burner with detailed chemistry", *Proceedings 9th U.S. National Combustion Meeting,*, Cincinnati, Ohio, USA., 2015, May 17-20.
[21]Eckel, G., Rachner, M., Le Clercq, P. and Aigner, M. "Semi-empirical model for the unsteady shear breakup of liquid jets in cross-flow," *Atomization and Sprays*, Vol 26, No. 7, 2016, pp. 687-712.
[22]Lempke, M., Gerlinger, P., Aigner, M. and Rachner, M. "Steady and unsteady RANS simulations of cryogenic rocket combustors", *AIAA*, Orlando, Florida, USA, 2011, January 4-7, pp. AIAA 2011-101.
[23]Rauch, B., Le Clercq, P., Aigner, M., Rachner, M., Calabria, R. and Massoli, P. "Jet A-1 fuel evaporation in a turbulent flow: Experimental investigations and validation of numerical models", *AIAA*, Orlando, Florida, USA, 2011, January 4-7, pp. AIAA 2011-790.
[24]Menter, F. R. "Two-equation eddy-viscosity turbulence models for engineering applications," *AIAA Journal*, Vol 32, No. 8, 1994, pp. 1598-1605.
[25]Blümcke, E., Brandt, M., Eickhoff, H. and Hassa, C. "Particle dispersion in highly swirling, turbulent flows," *Part. Part. Syst. Charact.*, Vol 10, No. 1993, pp. 182-190.
[26]Abramzon, B. and Sirignano, W. A. "Droplet vaporization model for spray combustion calculations," *International Journal of Heat Mass Transfer*, Vol 32, No. 1989, pp. 1605-1618.
[27]Dandy, D. S. and Vosen, S. R. "Numerical and Experimental Studies of Hydroxyl Radical Chemiluminescence in Methane-Air Flames," *Combustion Science and Technology*, Vol 82, No. 1-6, 1992, pp. 131-150.
[28]Lee, J. G. and Santavicca, D. A. "Experimental Diagnostics for the Study of Combustion Instabilities in Lean Premixed Combustors," *Journal of Propulsion and Power*, Vol 19, No. 5, 2003, pp. 735-750.
[29]Chen, Y.-C., Stårner, S. H. and Masri, A. R. "A detailed experimental investigation of well-defined, turbulent evaporating spray jets of acetone," *International Journal of Multiphase Flow*, Vol 32, No. 4, 2006, pp. 389-412.
[30]Ferrand, V., Bazile, R. and Borée, J. "Measurements of concentration per size class in a dense polydispersed jet using planar laser-induced fluorescence and phase Doppler techniques," *Experiments in Fluids*, Vol 31, No. 6, pp. 597-607.
[31]Ferrand, V., Bazile, R., Borée, J. and Charnay, G. "Gas–droplet turbulent velocity correlations and two-phase interaction in an axisymmetric jet laden with partly responsive droplets," *International Journal of Multiphase Flow*, Vol 29, No. 2, 2003, pp. 195-217.
[32]Nijdam, J. J., Stårner, S. H. and Langrish, T. A. G. "An experimental investigation of droplet evaporation and coalescence in a simple jet flow," *Experiments in Fluids*, Vol 37, No. 4, 2004, pp. 504-517.
[33]Gounder, J. D., Kourmatzis, A. and Masri, A. R. "Turbulent piloted dilute spray flames: Flow fields and droplet dynamics," *Combustion and Flame*, Vol 159, No. 11, 2012, pp. 3372-3397.
[34]Masri, A. R. and Gounder, J. D.,Details and Complexities of Boundary Conditions in Turbulent Piloted Dilute Spray Jets and Flames edited by *Experiments and Numerical Simulations of Diluted Spray Turbulent Combustion, ERCOFTEC Series 17.*, 2011. pp. 41-68.
[35]Lefebvre, A. H. and Ballal, D. R., *Gas Turbine Combustion - Alternative Fuels and Emissions*, 3rd ed., CRC Press, 2010.
[36]Tanner, F. X. "A cascade atomization and drop breakup model for the simulation of high-pressure liquid jets," 2003, pp. SAE-paper No. 2003-01-1044.
[37]Chin, J. S. and Levebvre, A. H. "Some comments on the characterization of drop-size distribution in sprays," *International Journal of Turbo and Jet Engines*, Vol 3, No. 1986, pp. 293-300.
[38]Morley, C., Gaseq - A chemical equilibrium program for Windows, version 0.79, www.gaseq.co.uk.